electronics

Article

An Intelligent Detection Method for Obstacles in Agricultural Soil with FDTD Modeling and MSVMs

Yuanhong Li [1,2], Congyue Wang [1], Chaofeng Wang [1], Yangfan Luo [3,4,*] and Yubin Lan [1,2,*]

[1] College of Electronic Engineering, South China Agricultural University, Guangzhou 510642, China; liyuanhong@stu.scau.edu.cn (Y.L.)
[2] Department of Biological and Agricultural Engineering, Texas A&M University, College Station, TX 77843, USA
[3] College of Engineering, South China Agricultural University, Guangzhou 510642, China
[4] Ministry of Education Key Technologies and Equipment Laboratory of Agricultural Machinery and Equipment in South China, South China Agricultural University, Guangzhou 510642, China
* Correspondence: luoyangfan@stu.scau.edu.cn (Y.L.); ylan@scau.edu.cn (Y.L.); Tel.: +86-13922707507 (Yubin Lan)

Abstract: Unknown objects in agricultural soil can be important because they may impact the health and productivity of the soil and the crops that grow in it. Challenges in collecting soil samples present opportunities to utilize Ground Penetrating Radar (GPR) image processing and artificial intelligence techniques to identify and locate unidentified objects in agricultural soil, which are important for agriculture. In this study, we used finite-difference time-domain (FDTD) simulated models to gather training data and predict actual soil conditions. Additionally, we propose a multi-class support vector machine (MSVM) that employs a semi-supervised algorithm to classify buried object materials and locate their position in soil. Then, we extract echo signals from the electromagnetic features of the FDTD simulation model, including soil type, parabolic shape, location, and energy magnitude changes. Lastly, we compare the performance of various MSVM models with different kernel functions (linear, polynomial, and radial basis function). The results indicate that the FDTD-Yee method enhances the accuracy of simulating real agricultural soils. The average recognition rate of the hyperbola position formed by the GPR echo signal is 91.13%, which can be utilized to detect the position and material of unknown and underground objects. For material identification, the directed acyclic graph support vector machine (DAG-SVM) model attains the highest classification accuracy among all soil layers when using an RBF kernel. Overall, our study demonstrates that an artificial intelligence model trained with the FDTD forward simulation model can effectively detect objects in farmland soil.

Keywords: machine learning; soil physics; FDTD; SVMs; multi-classification

Citation: Li, Y.; Wang, C.; Wang, C.; Luo, Y.; Lan, Y. An Intelligent Detection Method for Obstacles in Agricultural Soil with FDTD Modeling and MSVMs. *Electronics* **2023**, *12*, 2447. https://doi.org/10.3390/electronics12112447

Academic Editors: Padma Iyenghar and Elke Pulvermüller

Received: 30 March 2023
Revised: 24 May 2023
Accepted: 25 May 2023
Published: 29 May 2023

1. Introduction

Electromagnetic wave detection is a non-invasive object detection technique widely used in agriculture [1]. The classification or analysis of radar signals in terms of differences in electromagnetic properties has become a key research issue [2–4], because the modeling of agricultural soil requires efficiency and precision in order to provide the elusive physical parameters needed to meet the requirements of artificial intelligence algorithms that require multi-sample supervised learning. Artificial intelligence methods can quickly locate objects through GPR image processing, but it is very difficult to collect unknown sample characteristics, such as the electrical conductivity and water content of an object in actual farmland soil [5]. Our proposed solution to address this issue involves utilizing the FDTD simulation method to replicate the actual physical conditions of the soil environment. Additionally, we aim to enhance the precision of GPR signal classification by tackling the multi-classification problem through SVM. In their analysis of electromagnetic scattering from inhomogeneous dielectrics, Taylor and Castillo [6] proposed a straightforward boundary absorption interpolation method using the FDTD simulation method. The absorption effect of the boundary in FDTD forward modeling can directly affect the calculation accuracy and image quality and reduce the interference of FDTD boundary reflection echo. De-shan et al. [7] used C language and VC++ to develop a 2D forward modeling software for ground penetrating radar based on the finite difference time domain method. The differential formula of the DB2-MRTD algorithm is derived, and a multi-resolution time-domain (MRTD) forward modeling program is developed. Teixeira and Chew [8] used FDTD to simulate the propagation of electromagnetic waves in dispersive soil, and compared their findings with many experimental results to verify that FDTD can effectively simulate the propagation of electromagnetic waves in dispersive media.

To enhance the effectiveness of buried object detection using GPR while reducing the occurrence of false positives, several researchers have employed intelligent detection techniques, including machine learning [9–15]. Common classification methods include discriminant analysis, k-nearest neighbors [16], Bayesian classifiers [17], neural networks (ANN) [18,19], HMM [20–22], Random Forest [23] and Support Vector Machine (SVM) etc. [24,25]. Among them, support vector machine (SVM) is a binary correlation classifier that can be used for classification and regression analysis. The fundamental concept involves creating a hyperplane that can effectively divide data into two distinct classes with the greatest possible margin, and was originally introduced by Cortes and Vapnik [26]. After continuous improvement, the two-class SVM can no longer meet many classification requirements, so the multi-class SVM has been widely developed and applied [27]. Keskes and Braham [28] proposed a new method associated with Recursive Undecimated Wavelet Packet Transform (RUWPT) and Directed Acyclic Graph Support Vector Machine (DAG SVM) to solve classification problems [29]. Xie et al. [30] proposed a new method to identify GPR images of reinforced concrete structures and automatically identify voids using the SVM algorithm. Dinh et al. [31] combined traditional image processing techniques with deep convolutional neural networks to locate pixels of steel bar peaks; in the end, higher accuracy was obtained, but the algorithm did not account for its scalability. The effectiveness of the algorithm can only be used to detect specific objects. In their study, Karem and Frigui [32] suggest enhancements to edge histogram detectors that aim to decrease the occurrence of false positives. Their approach involves training Likelihood K-Nearest Neighbors or SVM classifiers on data acquired by a GPR sensor-equipped mine detector mounted on a vehicle.

The objective of this study is to develop a semi-supervised algorithm based on MSVM to create a GPR signal classification model. The model should be efficient enough to accurately categorize GPR signals from buried objects made of various materials, even when limited GPR data is available for training. The FDTD method can effectively replicate the true physical environment of soil, enabling the capture of specific information about various buried objects such as their material composition, positioning, and parabolic shape. By analyzing the amplitude, phase, and other signal characteristics of GPR, the MSVM is employed to classify different soil buried objects. In this study, various kernel functions were evaluated, and the optimal MSVM model was selected. The results demonstrate that this technology has great potential in agriculture, allowing for the detection of buried objects in soil, thus enhancing the efficiency of farmland operations and promoting a positive impact on the environment.

2. Materials and Methods

2.1. Experimental Preparation

The object detection study utilized the 2D module of gprMax to produce 210 GPR images, using the bowtie-shaped MALA 1.2 G antenna model as the benchmark [33]. The GPR frequency was set to 5 GHz, with time steps set to 3×10^{-12} and a time window of 5×10^{-9}. Out of the 210 images, 180 were used as material training sets, and the remaining 30 were used as material test sets [34]. The simulated soils distribution map was based on the US Department of Agriculture (USDA) soils classification criteria [35]. The electrical conductivity of soil can be influenced by factors such as soil salinity, moisture, temperature, organic matter, and texture content. Additionally, the soil's clay content, interfacial polarization, and water content can significantly impact its dielectric constant [36,37]. This study chooses three types of soil and compares them with an FDTD simulation. The first simulated soil is sand marked as "T_a" in this paper. The second one is clay, marked as "T_b"; The third one is silt, marked as "T_c". In the soil obstacle verification experiment, the relative permittivity of the soil ranged from 5 to 30, and the conductivity ranged from 0.01 to 0.5 ms/cm.

In this work, the prediction models for buried objects in soils were divided into five categories: glass sheets, PVC plastics, wood blocks, dry hard stones, and metal ores. Before burying, the distance from the soil surface to the depth of 5 types of soil obstacle materials was measured, and then, the experimental operation was to attempt detection by dragging the GPR in different soil environments, as shown in Figure 1.

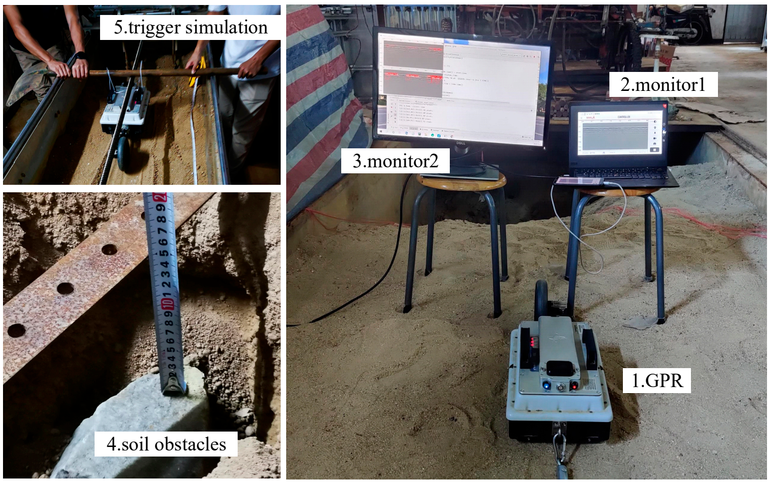

Figure 1. Experimental Environment and Equipment.

After collecting the GPR data, as shown in Figure 2, we calibrate the speed by first acquiring the time window parameters. Next, we adjust the blue curve in the figure by clicking on the vertex position of the parabola with the mouse and performing shape fitting. By doing so, we obtain the precise propagation speed of electromagnetic waves in the soil and the depth location of the abnormal signal.

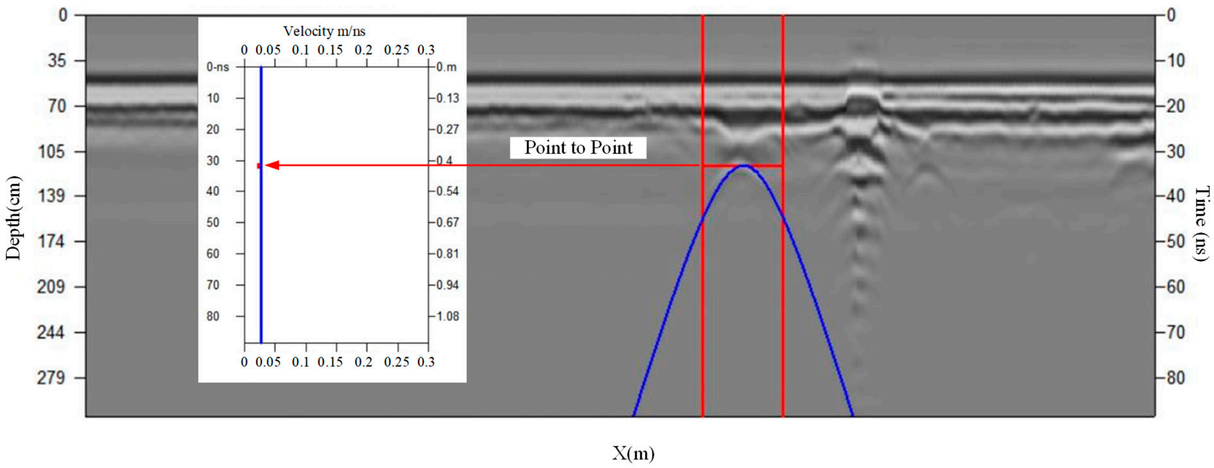

Figure 2. Velocity (depth) scaling of geometric features.

In the experiment, the media categories were numbered 1, 2, 3, 4, and 5, respectively, as shown in Table 1. The dielectric constant of the glass pieces ranges from 1.1 to 2.2, and its conductivity is between 0.001 and 0.01 s/m. The dielectric constant of wood materials is between 2.8 and 3.0, and its conductivity is between 0.0001 and 0.001 s/m. The PVC plastic block has a dielectric constant of between 3.0 and 8.0 and a conductivity value between 0.001 and 0.01 s/m. The dielectric constant of dry hard stone is between 6.0–12.3 and its conductivity is between 10×10^{-6} to 10×10^{-8}. The last material is metal block or ore, with a dielectric constant greater than 500, and is totally conductive.

Table 1. Conductivity and dielectric constant of five typical tillage soils objects.

Sample NO.	Category	ε_x	μ_x (s/m)	Velocity (m/μs)
1	Glass	1.1–2.2	0.001–0.01	150–200
2	Wood	2.8–3.0	10^{-4}–10^{-3}	112–122
3	PVC plastic	3.0–8.0	0.01–0.001	170
4	Stone	6.0–12.3	10^{-6}–10^{-8}	134
5	Mental	>500	/	Close light speed

2.2. Maxwell's Equation and FDTD Simulation Principle

The basic idea of FDTD is to use a central difference quotient to replace the first-order partial quotient of field quantity with respect to time and space. It can directly simulate very rich electromagnetic field problems with time domain information, and simplify the complex soil layer medium physical process into a mathematical difference or electromagnetic format parameters [38]. When solving the actual model, the relationship between field quantities obeys the six rotation equations of the Maxwell equation. In this way, geometric space problems can be solved by separation into orthogonal spatial grid points. The electric and magnetic fields were classified and placed in spatially discrete positions with excitation sources. Therefore, FDTD relies on Maxwell's principle to decompose its discrete three-dimensional geometric structure problem in the medium into Yee units. As shown in Figure 3, H (A/m) represents the magnetic field strength; E (V/m) represents the electric field strength; where i, j, k represents a three-dimensional coordinate position in space.

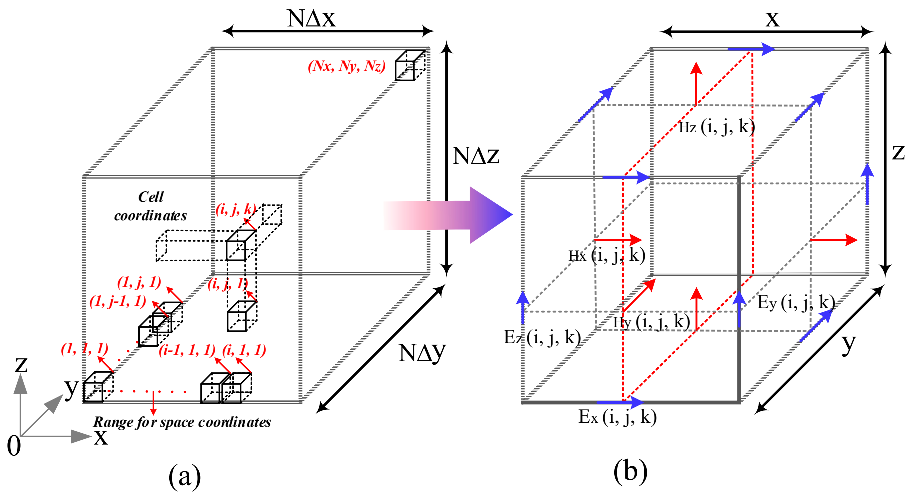

Figure 3. Magnetic field components in Yee cells (**a**) and Distribution of electric (**b**).

In the two-dimensional structure of FDTD, since a certain coordinate has no numerical change in direction, for example, the coordinate value on the Z axis of the constructed model in this paper was fixed in the XYZ coordinate system. The partial derivative associated with this coordinate exists. Obviously, the electromagnetic classification in the two-dimensional case can be divided into two independent groups, such as E_x, E_y, and H_z as a group that can be denoted as TE electromagnetic field group (formula (1) and (2)). Similarly, E_z, H_x, and H_y can be denoted as TM electromagnetic field group (formula (3) and (4)). This FDTD equation can be simplified into two-dimensional problems. The TE formula for E_x, E_y electromagnetic field is:

$$\begin{cases} \frac{\partial E_x}{\partial t} = \frac{1}{\varepsilon}\left(\frac{\partial E_x}{\partial t} - \partial E_x - J_x\right) \\ \frac{\partial E_y}{\partial t} = \frac{1}{\varepsilon}\left(\frac{\partial H_x}{\partial x} - \partial E_y - J_y\right) \end{cases} \tag{1}$$

The TE formula for Hz electromagnetic field is [39]:

$$\frac{\partial H_z}{\partial t} = \frac{1}{\varepsilon}\left(\frac{\partial E_x}{\partial y} - \frac{\partial E_y}{\partial x}\right) \tag{2}$$

where, σ (S/m) represents the medium's conductivity; ε (F/m) represents the dielectric constant of the medium; represents the permeability of the medium; J (A/m^2) is the current density. The TM formula for H_x, H_y electromagnetic field is:

$$\begin{cases} \frac{\partial H_x}{\partial t} = -\frac{1}{\varepsilon\mu}\frac{\partial E_z}{\partial y} \\ \frac{\partial H_y}{\partial t} = \frac{1}{\mu\varepsilon}\frac{\partial E_z}{\partial x} \end{cases} \tag{3}$$

The TM formula for E_z electromagnetic field is:

$$\frac{\partial E_z}{\partial t} = \frac{1}{\varepsilon}\left(\frac{\partial H_y}{\partial x} - \frac{\partial H_x}{\partial y} - \sigma E_z - J_z\right) \tag{4}$$

2.3. Simulated Experiment Setup and Evaluation

The SVM's training process used python 3.7 and the model name is "ScikitLearn", which is a machine learning library in python [40]. The total size of the FDTD 3D model is set to 240 × 210 × 120 mm, and the base model is set to 240 × 210 × 2 mm, which represents the X, Y, and Z directions, respectively. In the 3D model, we divide the data model into 24 slices, the total time depth is 32.21 ns, the distance depth is 0.4 m, and the number of samples is 148. The velocity of the model is 0.025 m/ns, the effective time window is 88.66 ns, and the binary value is 128. The soil's object position prediction from GPR images can be converted to an image processing problem. As depicted in Figure 4, the output is produced by gprMax's B-scan module and the objects in GPR images are identified based on the propagation of pulse signals, resulting in features such as hyperbolic curves, linear segments, and electrical impedances. Figure 4a below shows a schematic diagram of the detected soil objects generated by ParaView 5.6.0 (regular-shaped rectangular parallelepiped as an example). According to the procedures described in Section 2.1, we composed the FDTD grid space by electromagnetic field as a cube of 0.240 m × 0.20 m × 0.002 m. The rectangular frame forms a perfect matching layer (PML) with a thickness of 0.02 m. Where the label "Air" means an air layer with a height of 0.03 m. The simulated radar transmitter probe is marked "TX" and the receiver probe is marked "RX". The length, width, and height of the object are known. The B-scan GPR image in Figure 4b exhibits a hyperbolic pattern that can be characterized by various parameters. C_0 represents the horizontal position of the apex and the vertical position of the apex can be equal to (0.17 m − Z_t + Z_m). Point P is the coordinates of the hyperbolic vertex. β represents the slope of the hyperbola asymptotes. Z_t is the depth from the top surface of the object to the ground, and Z_m is the distance from the hyperbolic apex to the upper surface of the object. Points A (a1, b1), B (a2, b2) and P in Figure 4b belong to the geospatial coordinates system.

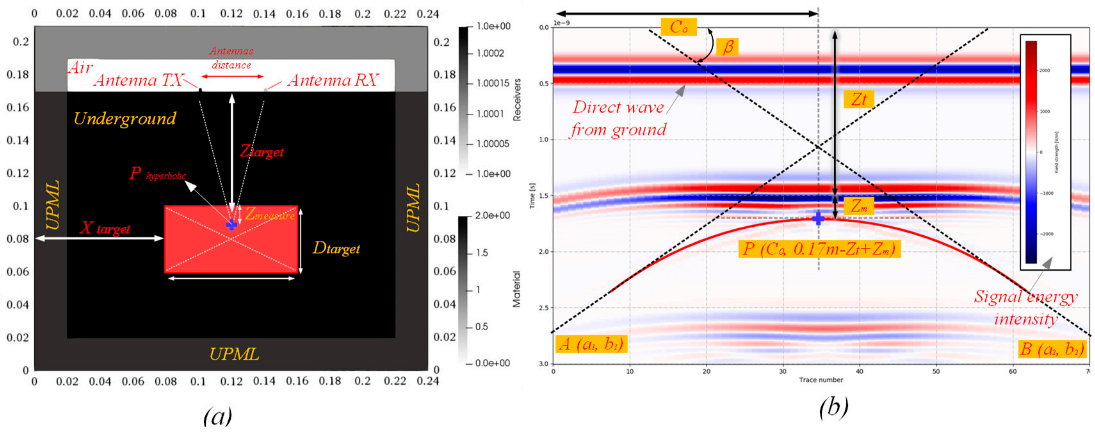

Figure 4. FDTD simulated magnetic field space: figure (**a**) illustrates the soil objects that were detected using ParaView 5.6.0, with a regular-shaped rectangular parallelepiped being used as an example. Figure (**b**) exhibits a hyperbolic pattern that can be characterized by various parameters.

Afterwards, the FDTD was meshed and its boundaries were converted into a grayscale image in the hyperbolic pattern of a B-scan. Here, we used the Hough transform algorithm to identify the target contour [41–44]. In B-scan maps, the echoes of electromagnetic waves appear as hyperbolic or approximate hyperbolic, and their positional relationship can be expressed as the following equation:

$$\frac{t^2}{t_0^2} - \frac{4 * \left(x - c^2\right)^2}{\left(v * t_0\right)^2} = 1, \tag{5}$$

and $t_0 = 2 * \frac{0.17 - \mathrm{Zt} - \mathrm{Zm}}{\mathrm{v}}$, where $0.17 - Zt - Zm$ is the target's depth; t means signal traveling time; v represents the propagation speed of electromagnetic waves. To be discretized, the hyperbolic Equation (1) can be expressed as $\frac{j_2}{j_0^2} - \frac{(i-i_0)^2}{\frac{v}{2j_0 d_c \ d_t}} = 1$, where $t_j = jd_t, C_i = id_c$, $C_0 = i_0 d_c$, $t_0 = j_0 d_t$, the coordinates of the hyperbolic vertices are i_0 and j_0 [45]. To extract the region of interest for Hough algorithm accumulation, we composed it by the vertex coordinate (i_0, j_0). The transformation equation of the Hough algorithm can be calculated by (6).

$$\mathrm{H}(i_0, j_0) = \sum_{i_{x_1}}^{i_{x_N}} \sum_{j_{x_1}}^{j_{x_n}} I(i,j) Q(i,j) \tag{6}$$

where $Q(i,j)$ is the gray value function. Obviously, according to the distribution between $H(i_0, j_0)$, we can estimate the object hyperbolic vertex position.This can be defined as $C_0 \in [0, n_{trace}]$, where n_{trace} is the number of traces in the GPR image. Where $Z_t \in \left[0, T_{depth}\right]$ and $Z_m \in \left[0, T_{depth}\right]$. T_{depth} is the depth perpendicular to the ground, which is measured as the length of the time windows. The range of the β belongs to $\beta \in \left[0, \frac{\pi}{2}\right]$. When the gray image is obtained, we mark the hyperbola vertices P in the hamming distance of the coordinate system and encode them into a binary image. The general steps can be divided into: (1) Searching for a hyperbolic contour from the generated sample GPR image. (2) Selecting the optimal segmentation threshold based on the edge detection. (3) Extracting the hyperbolic characteristic of the electromagnetic signal. (4) Image binary coding. (5) End the image processing flow and output local coordinates. (6) Convert position coordinates to geospatial coordinates. (7) Predict hyperbolic contours of known materials based on partial parameters. Finally, we simulate realistic soil with a stochastic distribution of dielectric properties constructed by Yee units of the FDTD geometry mesh [46]. The sand fraction, clay, and silt fraction are set according to the parameters described in Section 2.1. The bulk density of soils is 2 g/cm^3. The volumetric water fraction range was 0.001–0.25. Its roughness is set among a range of 3–8 mm [47]. The soil's fractal weight in the x, y and z direction ranges among 0.5–1. The fractal dimension values are between zero and three. Figure 5 shows the 3D heterogeneous soils layer that is constructed by the FDTD grid in the geometry view.

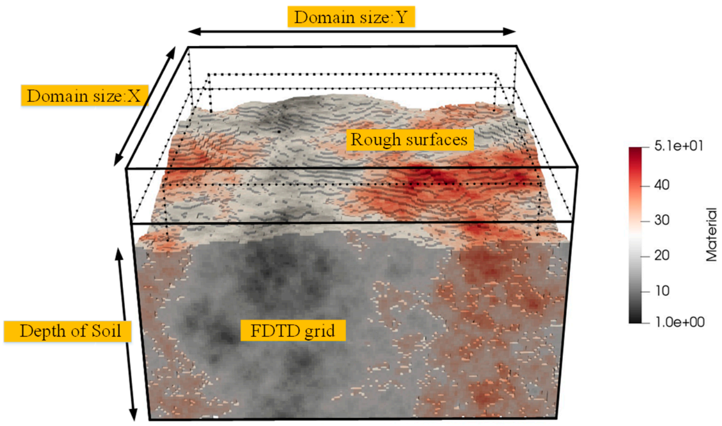

Figure 5. Soil layer simulation.

2.4. Principle of Multi-Classified SVM

SVMs can handle high-dimensional feature spaces, which can be beneficial when dealing with the large amount of data generated by electromagnetic signals and efficiently process and extract relevant features from the data to accurately classify different objects. It is evident that the majority of clustering methods are only capable of categorizing data that can be represented linearly in a limited number of dimensions. This means that SVMs can accurately classify the reflected intensity of electromagnetic signals, even in the presence of noise or incomplete data. Here is the math principle of the SVMs: let us say we have a set of data with an unknown distribution, given as $S = \left\{X_i^p\right\}_{i=1}^N \cup \left\{Y_j^g\right\}_{j=1}^N$, where X_i^p is the label of $X = \{(x_1, y_1), (x_2, y_2), \ldots (x_n, y_n)\}$, Y_i^g represents the unlabeled sample sets: $Y = \{y_n', y_n', \ldots y_n'\}$. We denoted i and j to be the identity number of the GPR signal from the testing groups [48,49]. The GPR image pair was constructed as $\left\{\left(X_i^p, Y_j^g\right), L_j^p\right\}$, where $L_j^p = 1$ means this sample is matched to the predicted data, while $L_j^p = -1$ indicates incorrect matches. Label Lx can be predicted accurately, as long as there is a sample-specific data set D_i^p, which is derived from $\left\{\left(X_1^p, Y_1^g\right), \ldots, \left(X_i^g, Y_N^g\right)\right\}$, so the binary classification equation can be expressed as:

$$D_i\left(X_i^P, X_j^g\right) = \begin{cases} \geq 0, L_j^p = +1 \\ \leq 0, L_j^p = -1 \end{cases} j = 1, \ldots, N \tag{7}$$

Suppose there is an n training vector here $x_i \in R^P$ $(i = 1, 2, 3 \ldots n)$, and the data set can be divided into two categories. Their labels $\in \{1, -1\}^N$. The basic SVM's model function can be represented as:

$$\min_{\omega, b, \varepsilon} \frac{1}{2} \omega^T \omega + C \sum_{i=1}^{n} \varepsilon_i \tag{8}$$

Subject to $y_i\left(\omega^T \varnothing(x_i) + \mathrm{b}\right) \geq 1 - \epsilon_i, (\epsilon_i \geq 0, \mathrm{i} = 1, 2 \ldots \ldots \mathrm{n})$, ω represents the normal vectors of the hyper-plane, and b means the bias variables, $\varnothing(x_i)$ is the higher dimensional space function, and $\in_i$ is the slack variables which violate the SVMs functional margin demands. When the penalty factor C > 0, the Lagrange function can be minimized as:

$$\mathrm{L}(\omega, b, \alpha, \beta) = \frac{1}{2}\omega^T\omega + \mathrm{C}\sum_{i=1}^{l}\varepsilon_i - \sum_{i=1}^{l}\beta_i\varepsilon_i - \sum_{i=1}^{l}\alpha_i\left[y_i\left(\omega^T\varnothing(x_i + b) - 1 + \varepsilon_i\right)\right] \tag{9}$$

where $\alpha = (\alpha_1, \alpha_2 \ldots, \alpha_l)^T$ and $\beta = (\beta_1, \beta_2 \ldots, \beta_l)^T$ are Lagrange multipliers enforced under condition $y_i(\omega^T\varnothing(x_i) + \mathrm{b}) \geq 1 - \epsilon_i, (\epsilon_i \geq 0, \mathrm{i} = 1, 2 \ldots\ldots \mathrm{n})$. To solve the optimization problem introduced by the Lagrange function, we need to minimize the function as:

$$\min_{\alpha}\frac{1}{2}\alpha^T Q\alpha - e^T\alpha \tag{10}$$

Which is subject to $y^T\alpha = 0, (0 \leq \alpha_i \leq \mathrm{C}, \mathrm{i} = 1, 2 \ldots \mathrm{n})$

The Q is an n × n positive semi-definite matrix, and C is denoted as the upper bound. e is the vector corresponding to the matrix. Where $Q_{ij} = y_i y_j K(x_i, x_j)$ and $K_{ij} = \varnothing(x_i)^T\varnothing(x_j)$ represent the core of kernel. The decision function is:

$$\mathrm{sgn}(\sum_{i=1}^{n} y_i\alpha_i K(x_i, x) + \rho) \tag{11}$$

This is a ridge regression algorithm, where C can be denoted as $C = 1/\alpha$, and ρ is the intercept of the support vector function. The classification of objects buried in farmland is not limited to just two categories. In fact, there are three MSVM methods that are commonly used for multivariate classification problems: DAG, one against one (OVO), and one against all (OVA). The OVA approach involves creating a binary SVM classifier for each category and labeling samples as "positive" if they belong to that category, and "negative" if they belong to any other category. For instance, if there are five different types of materials, the first SVM classifier would mark all positive samples that belong to category 1 and treat other categories as negative samples. Similarly, a second SVM classifier would be constructed for category 2 as positive samples and negative samples for other categories. For N samples, N SVM classifiers would be required. The OVO strategy can be used to transform a multiclass classification problem into a binary classification problem. Two categories from all categories are chosen arbitrarily, then, such steps are repeated until all of the different paired sets of categories correspond to one SVM trainer [50]. Therefore, N samples correspond to N (N − 1)/2 SVM models. After the final class of test samples is determined by N (N − 1)/2 binary SVM classifiers, the score matrix is as follows:

$$\mathrm{R} = (r_{ii})_{n\times n} = \begin{Bmatrix} r_{11} & r_{12} & \cdots & r_{1n} \\ r_{21} & r_{22} & \cdots & r_{21} \\ \vdots & \vdots & \vdots & \vdots \\ r_{n1} & r_{n2} & \cdots & r_{nn} \end{Bmatrix} \tag{12}$$

where $r_{ii} \in [0,\ 1]$ is the binary classifier's confidence, i and i' are the discrimination class. The sample training phase of the DAG model is similar to OVO, but in its test phase, it has N (N − 1)/2 internal nodes and (N − 1) leaves, similar to a DAG tree generated for a multi-class problem [51]. The DAG will generate a multi-level two-class SVM classifier until all of the last leaf nodes reach out.

2.5. SVM Kernel Function Selection

Applying GPR image feature mapping to the SVM classification, it makes the inner product $\left(x^{(i)}, x^{(j)}\right)$ of $\omega^T\mathrm{x} + \mathrm{b}$ map into $\left(\varnothing\left(x^{(i)}\right), \varnothing\left(x^{(j)}\right)\right)$. The kernel implicitly converts two vectors to other forms and then finds the inner function. Where $\mathrm{K}(x_i, x_j) = \varnothing(x_i)^T\varnothing(x_j)$ is called the kernel function. Assuming that x_i and x_j are n-dimension, but the actual demand needs to be mapped into n^2 dimension, the $K(x_i, x_j)$ can be obtained from equation $K(x_i, x_j) = \varnothing(x_i)^T \varnothing(x_j)$. Its matrix K is a symmetric matrix. Any vector Z here has the relationship of $z^T K z = \sum_k \left(\sum_i z_i \varnothing_k \left(x^{(i)}\right)\right)^2$. Obviously, the square of the original feature x_i and x_j inner product is calculated in advance by the dimensionality reduction kernel function, thereby saving computation time. Here, training vectors x_i are mapped into a higher (probably infinite) dimensional space by the function Φ. This article chooses three Kernel functions for comparison: Linear, polynomials (POLY), and RBF. The linear kernels can be formed as $K(x_i, x_j) = x_i^T x_j$. For degree-d polynomials, the polynomial kernel is defined as:

$$K(x_i, x_j) = (x_i^T x_j + c)^d \tag{13}$$

x_i and x_j are a vector form of the input data. When C = 0, this kernel is called homogeneous; the corresponding feature dimension here is $(n + d,\ d)$. Suppose that d = 2, we can deduce the special quadratic kernel with multinomial theorem:

$$K(x_i, x_j) = \sum_{i,j=1}^{n} \left(x_i^2\right)\left(x_j^2\right) + \sum_{i=2}^{n} \sum_{j=1}^{i-1} \left(\sqrt{2} x_i x_{i-1}\right)\left(\sqrt{2} x_j x_i\right) + \sum_{i-1}^{n} \left(\sqrt{2c} x_i\right)\left(\sqrt{2c} x_j\right) + c^2 \tag{14}$$

Gaussian kernel, also known as the radial basis function (RBF). In general, RBF has only three layers in a neural network, in which there is no weight connection from the input layer to the hidden layer, but the distance or similarity between different layers can be calculated directly by the hidden layer [52]. Since the RBF network is only connected by the weights between the hidden layers to the output layer, the training speed is faster than nonlinear functions such as sigmoid [53]. The form of the original RBF kernel is $e^{-r\|x_i - x_j\|}$ as the binary classifier [54]. Its multiple form implements as:

$$K(x_i, x_j) = \exp\left(-\frac{\| X_i - X_j \|^2}{2\sigma^2}\right) \tag{15}$$

where $\| x_i - x_j \|^2$ is called the squared Euclidean distance between the two feature vectors; σ is a free parameter and stands for the window width; r represents the kernel parameter selected by cross-validation, and $\gamma = \frac{1}{2\sigma^2}$. For $\sigma = 1$, the RBF equation is:

$$\exp\left(-\frac{1}{2} \| x_i - x_j \|^2\right) = \sum_{n=0}^{\infty} \frac{\left(x_i^T, x_j\right)^n}{n!} \exp\left(-\frac{1}{2} \| x_i \|^2\right) \exp\left(-\frac{1}{2} \| x_j \|^2\right) \tag{16}$$

2.6. Workflow of Data Processing

We first conduct FDTD object modeling for five different materials. Then, we set up the soil and position parameters. Next, we use GPR for detection at the same soil depth. The experiment is divided into two parts, as shown in Figure 6. One part involves modeling using gprMax software in the laboratory, while the other part involves detection using instruments. The required parameters will be obtained based on the same external conditions. The dataset for semi-supervised learning includes both labeled and unlabeled data. For example, in this study, we correlate Emax and Pmax with the material type X. We use known material types as labeled data and apply SVM classification to unknown material types. After training, MSVM can predict simulation data and real data.

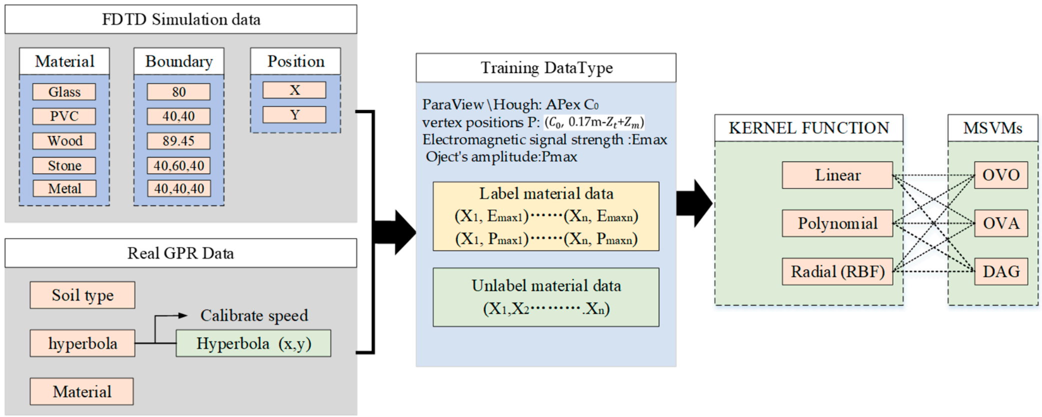

Figure 6. Data Processing Workflow.

3. Results and Discussion

3.1. Performance and Evaluation of Position Prediction

To get the specific position and value from ParaView, we load our simulation data and create the visualization. Then, we select the "Selection" tool, click on the "Pick Data" button, and select the point apex C_0. In the "Properties" panel, we expand the "Information" section to view the X, Y, and Z coordinates of C_0. To get the value of the data at the selected point, we expand the "Display" section and find the variable under "Cell Data" or "Point Data". Finally, the value of the variable at the selected point will be displayed. As shown in Figure 7, there are two ways to compare apex C_0, ParaView 5.6.0 (FDTD) and Hough contour recognition, calculated by the S equation. The solid blue line represents the outputs of the C_0 value in ParaView, and the red dashed line represents the calculated value of the contour recognition. A total of 15 samples were tested here, and the values of C_0 in the 2nd, 3rd, and 4th samples were slightly inaccurate. The two sets of data were very close. This proves the validity of the Hough transform combine with S equation method for detecting hyperbolic contours.

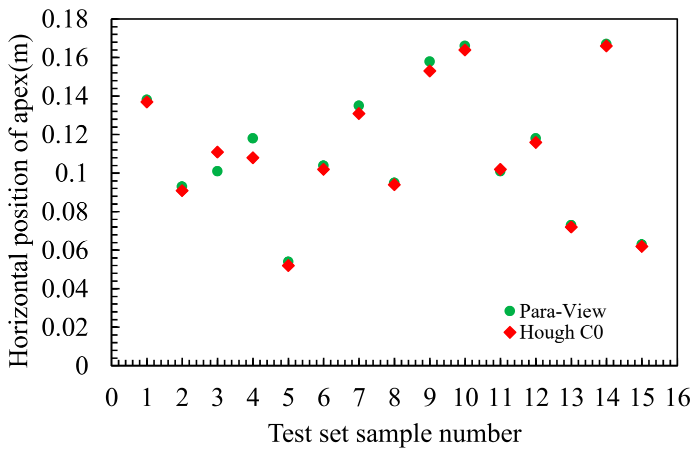

Figure 7. Horizontal position of apex in ParaView and Hough.

The ParaView and Hough algorithms are used to calculate point A (a1, b1) and point B (a2, b2) of Figure 4, respectively. The five materials are: Plastic (P), Stone (S), Wood (W), Glass (G), and Iron (I). "OT" represents the object's type and Ta, Tb, and Tc represents three types of soils with different conductivity and dielectric constants. We use Reflexw to obtain the stratification in soil [55]. Figure 8 shows the stratification of soils after channel tracking of GPR images. It can be see that accuracy of our method for calculating the hyperbolic position based on the Hough transform and the "S equation" is ideal. When the soil type is Tc, the plastic recognition rate of the hyperbolic position can reach 98.44%.

When the soil type is Ta, the recognition rate of wood materials is also 82.66%. Overall, the average recognition rate is about 91.13%, which indicates that the proposed GPR hyperbolic recognition method, which is based on Hough image processing, is effective and feasible, and it can generally be applicable to different types of soil layers.

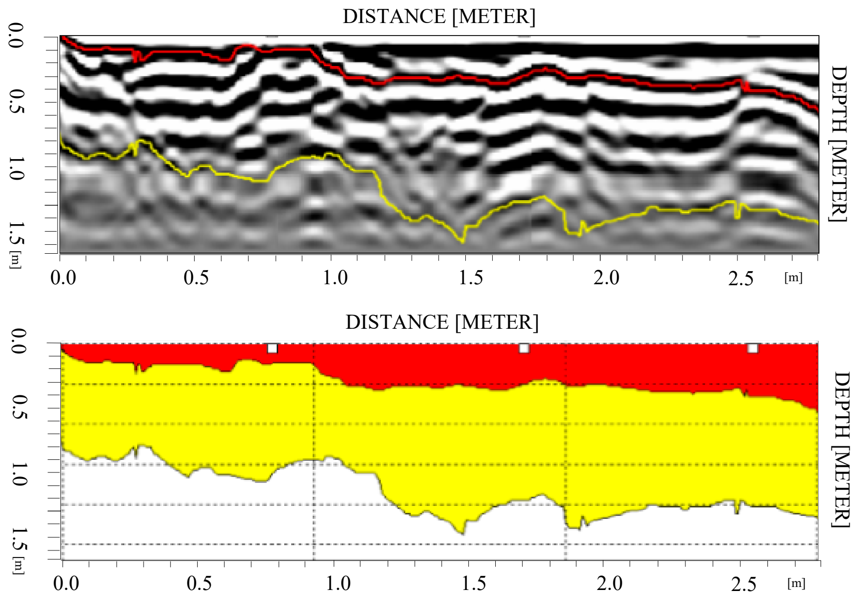

Figure 8. Soil stratification in GPR images (red color means the first soil layer, yellow color means the second soil layer).

3.2. Material Identification with FDTD

Feature labels of SVMs include the object dielectric constant, highest amplitude values, lowest amplitude values, magnetic loss and conductivity. Table 2 shows the model accuracy of FDTD models at gprMax. Model accuracy was obtained by comparing the data between the model real values and SVM prediction values. Here, we adopted the Mean Absolute Error (MAE) to evaluate the method performance. We can find from Table 2 that the lowest MAE boundary prediction was 0.21, and its corresponding object depth error was 0.82 mm. In addition, it can be seen in the MAE data of the depth prediction that its minimum value was 0.15. This indicates that the simulation can perform with high accuracy under the FDTD prediction.

Table 2. FDTD simulation and estimated result of different boundary sizes and depths.

Model	Test Boundary Size (mm)	Center Position Deviation (m)	Test Middle Depth Size (m)	Calculated Boundary Size	Calculated Middle Depth	MAE (Boundary)	MAE (Depth) (mm)
a	80	0.117	0.07	79.63	0.0715	0.37	0.15
b	40, 40	0.123	0.07	39.42, 38.17	0.0698	0.58	0.21
c	89.45	0.119	0.09	88.82	0.0896	0.63	0.43
d	40, 60, 40	0.121	0.10	40, 59.23, 39.98	0.1003	0.42	0.31
e	40, 40, 40	0.120	0.07	39.99, 39.87, 39.65	0.0692	0.21	0.83

The reflected intensity (amplitude) of the electromagnetic signals from objects in agricultural soils directly reflects their material properties [56,57]. In this research, we examined the electromagnetic properties of the five most commonly found materials in farmland soil: PVC plastic, stone, wood, glass, and metal. We illustrate the energy amplitude diagrams for each of these materials and use two features to analyze the electromagnetic signals: the maximum value of electromagnetic signal strength (Emax) and the maximum value of the object's amplitude (Pmax) in the spectral range. We concluded that the energy amplitude of PVC plastic demonstrated an Emax of 0.00532 and a Pmax of 0.965. PVC plastic exhibits a clear response to electromagnetic signals. The energy amplitude for dry hard stone is an Emax of 0.0009 and a Pmax of 0.0602. Dry hard stone has a relatively high magnetic loss, and its water content in farmland soil is almost zero, resulting in weak echo wave reflections due to its conductivity properties. The energy amplitude for wood is an Emax of 0.00462 and Pmax of 1.180. In the cube model, the wood block is a non-conductive material and contains some water in the farmland soil. Compared to stone, the surface of the wooden block shows stronger echo reflections. Glass is an amorphous, inorganic mineral consisting of Na2SiO3, CaSiO3, and SiO2. The electrical conductivity of glass is generally low but it can cause a more pronounced oscillation of the electromagnetic signal in the soil layer. Finally, conclusions can be drawn regarding the changes in energy amplitude for the metal block. Its E_{max} was 0.0178 and P_{max} was 1.190. Metal's conductivity was strong and could produce a strong reflection. In summary, each material differs in the change of energy amplitude. It is feasible to use the energy intensity of the object in the excitation source at different frequencies to distinguish their material, but it is not certain whether the difference in soil type will affect the spectral distribution of electromagnetic signals.

According to the USDA classification criteria, the soils were classified by the percentage of sand, clay, and silt content. The accuracy of two kernel functions for known targets which were under soil types T_a, T_b and T_c are shown in Table 3. The number of classifier-training samples were between 20 and 200. When the soil type was T_a, the average accuracy rate reached 88.15% as the number of training samples increased. Similarly, the average accuracy of T_b was 83.16%, and the average accuracy of T_c was 86.94%; thus, the model performance was $T_a > T_c > T_b$. Obviously, the RBF model is better than POLY. When the soil type was T_a, the average model accuracy rate can reach to 91.70%. Similarly, the accuracy of the T_b model is 90.28% and the accuracy of the T_c model is 86.04%. Overall, the model takes its performance as $T_a > T_b > T_c$.

Table 3. Accuracy rates of different soil types.

Soil Type	OT	ParaView (FDTD)		Hough		Accuracy (%)	Accuracy (%)
		Z_m (m)	Z_t (m)	Z'_m (m)	Z'_t (m)	Point A (a_1,b_1)	Point B (a_2,b_2)
Ta (sand:98.9%) (clay:9.53%)	P	0.005	0.148	0.004	0.146	87.82%	85.83%
	S	0.006	0.156	0.005	0.153	96.01%	85.84%
	W	0.007	0.089	0.0067	0.084	82.66%	86.59%
	G	0.002	0.149	0.002	0.147	92.28%	93.54%
	I	0.002	0.062	0.003	0.064	94.52%	94.08%
Tb (silt:23.40%) (clay:80.0%)	P	0.003	0.145	0.004	0.142	85.09%	89.45%
	S	0.006	0.098	0.004	0.101	89.68%	89.89%
	W	0.003	0.160	0.004	0.14	96.71%	87.62%
	G	0.005	0.127	0.006	0.127	94.11%	92.50%
	I	0.002	0.162	0.002	0.161	95.72%	97.62%
Tc (silt:70%) (sand:17.0%)	P	0.004	0.137	0.003	0.135	98.44%	86.67%
	S	0.007	0.152	0.006	0.148	94.63%	89.12%
	W	0.003	0.075	0.002	0.074	85.70%	91.43%
	G	0.008	0.120	0.006	0.115	91.03%	88.55%
	I	0.005	0.119	0.003	0.117	91.17%	97.54%

3.3. Performance and Evaluation of Material Recognition

For the vertex positions P (C_0, 0.17m $-$ Z_t + Z_m) of the five kinds of objects, the distance between the two points on the hyperbola and echo signal amplitude had been classified depending on the FDTD simulated results. Here, the "decision function" module in SK-learn was proposed to perform the scores and probabilities evaluation. This starting purpose for evaluation is to find some functions that are distinct between those five objects' materials. We adopted the root mean square (RMS) to evaluate the SVM algorithm's performance. RMS can be represented by:

$$\text{RMS} = \sqrt{\sum_{i=1,2\ldots N} \frac{\left(M_a^b(x)\right)^2}{N}} \quad (17)$$

N is the number of samples and M_a^b represents the matrix of the input vectors. The kernel functions in this procedure include: Linear, POLY (degree = 4), and RBF. Table 4 shows the material test results under three MSVM trainers with different kernel functions. In the linear model, the correct detection rate (CDR) of DAG was 92.04%. In the POLY model, the CDR of the OVA and DAG were relatively high: 90.11% and 92.94%, respectively. Obviously, in all MSVM models of the RBF kernel, the CDR of OVO, OVA, and DAG were 90.175, 94.73%, and 93.70%, respectively. As shown in the data analysis of training and decision time, it is obvious that DAG was more efficient than another kernel functions. For the identification of object materials, the RMS of DAG in the three kernel models were 0.13, 0.21, and 0.34. Compared with the OVO and OVA models, the DAG model has a stable recognition rate and can maintain a certain accuracy. The classification or recognition rate of OVO and OVA models fluctuated greatly.

Table 4. MSVM performance of different kernel functions.

Kernel Functions	MSVM	CDR [1]	Training Time (s)	Decision Time (s)	SVN [2]	RMS
Linear	OVO	79.89%	0.134	0.0072	132	0.21
	OVA	82.56%	0.263	0.0133	67	0.34
	DAG	92.04%	0.184	0.0089	89	0.13
POLY	OVO	82.23%	0.181	0.0084	120	0.28
	OVA	90.11%	0.090	0.0067	96	0.25
	DAG	92.94%	0.108	0.0074	107	0.21
RBF	OVO	90.17%	0.155	0.0055	77	0.21
	OVA	94.73%	0.218	0.0103	69	0.16
	DAG	93.70%	0.170	0.0029	152	0.34

[1] Correct Detection Rate (CDR), [2] Support Vector Number (SVN).

We experimented with various SVM algorithms using kernels. The linear kernel SVM is a linear classifier that can effectively identify linear features in object materials. However, overfitting can occur when the classifier considers noise data points as features, which disrupts the predefined classification rules. The linear SVM divides data into three categories, but the scalable linear classifier only divides data into one category in the area of empty values. On the other hand, the SVM with an RBF kernel demonstrated the best classification performance. The RBF kernel can classify different types of data nonlinearly and maximize classification accuracy. Additionally, the performance of SVM with polynomial kernel classification was also promising, but the appropriate "degree" needs to be adjusted. This algorithm can identify categories to the maximum extent but may not be able to classify them completely. The polynomial kernel functions with kernel functions of d = 3 and d = 5 were considered. Obviously, when d = 4, the classification performance was better than when d was 3 or 5. Linear was similar to RBF for classifying data in the case of linear separability. However, in the case of linear inseparability, the RBF model was significantly better than the linear and POLY models. For the classification of GPR signals constructed by FDTD, the RBF and POLY-MSVM classifier are the best in the nonlinear classification. Neural network with RBF as the kernel has no weight connection from the input layer to hidden layer, and only the weighted connection from the hidden layer to the output layer. Therefore, RBF was clearly better than POLY in their computational efficiency. On the other hand, the soils type of GPR is an important indicator that influences the difference of GPR signals in identifying the type of objects.

Table 5 shows the results of tests based on RBF kernel function trainer, where NCC stands for the number of correct classifications and NIC stands for the number of incorrect classifications. The testing samples consisted of 200 real GPR images. The number of correctly classified samples was 170 and the number of incorrect classified samples was 30. The highest recognition rate of object material is iron, because iron has a stronger reflection intensity of electromagnetic waves. Obviously, the dielectric constant and conductivity of plastic were similar, but when the object material is plastic, the recognition rate can still reach 89.58%. The recognition rate of glass was the lowest, which is related to the grid structure of the FDTD forward simulation. The recognition accuracy of stone was 81.81%. Dry hard stone was not obvious for electromagnetic wave absorption. Therefore, it is easily affected by the boundary signal noise in the RBF-SVMs model and can be predicted by classifier as other materials. Regarding the overall analysis for all models, the total recognition rate can reach 86.4%. This illustrates the superiority of the RBF-SVM model proposed in this paper.

Table 5. The RBF-SVM recognition results.

Material	Number of Images	NCC	NIC	Rate of Classification
Wood	31	27	4	87.09%
Plastic	48	43	5	89.58%
Iron	36	34	2	94.44%
Stone	55	45	10	81.81%
Glass	30	21	9	70.00%
Total	200	170	30	85.00%

3.4. ROC Curve and AUC Value

The electromagnetic wave signal is not readily observable in the soil surface layer. In this study, the signal in the Z section is marked, and sampling statistics are conducted on the electromagnetic wave amplitude data. For instance, data statistics of DAG-SVMs, OVA-SVMs, and OVO-SVMs are performed. To evaluate the performance indicators of the two-category machine learning model, we employ the receiver operating characteristic (ROC) and area under curve (AUC). The false positive rate (FPR) and true positive rate (TPR) are area values used to measure the model index performance in an algorithm. A perfect classifier exhibits TPR = 1 and FPR = 0 simultaneously. The value of AUC corresponds to the area covered by the ROC curve with the coordinate axis. A larger AUC indicates better classifier performance. Figure 9 illustrates the ROC curves of the three MSVM classifiers with RBF as the kernel function. The diagonal line in the middle of the coordinate system represents the prediction curve for "random guess". Curve 1 denotes the ROC curve of the OVO model. It can be observed that curve 1 ranges from $0.5 < AUC < 1$, but this ROC curve is still suboptimal. Compared to curve 2 and curve 3, it is apparent that the classifier performance of DAG-SVMs is superior to OVA and OVO. Furthermore, the AUC values of DAG-SVMs are also superior to OVA-SVMs and OVO-SVMs.

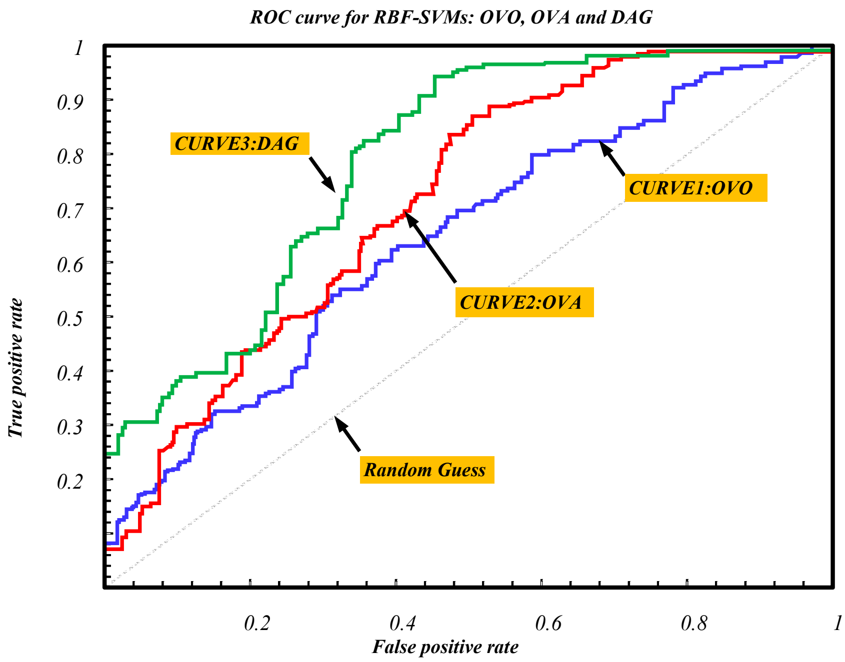

Figure 9. ROC curve for RBF-SVMs: OVO, OVA and DAG.

4. Conclusions

This research paper proposes a method of using multi-class support vector machines with artificial intelligence to identify and categorize objects beneath agricultural soil. The study introduces the FDTD model to generate the training data for the MSVM classifier, which ensures that the training results are applicable to actual agricultural soil and its layers. Furthermore, the model also includes dielectric objects commonly found in real-world agricultural settings. The study evaluates the MSVM classifier's performance metrics using various kernel functions. In conclusion, the research findings highlight that the proposed method can effectively detect and classify underground objects in agricultural soils with satisfactory performance, as demonstrated by the experimental results:

The FDTD-Yee method can improve the precision of simulating soil layers and their properties in real farmland. Detecting the position and material of unknown underground objects is made easier, with an average recognition rate of 91.13% for the hyperbola position formed by GPR echo signals.

Our proposed method for recognizing GPR images is a DAG method that utilizes the MSVM and RBF kernel. The effectiveness and superiority of this method have been demonstrated.

The FDTD simulation results reveal that the RBF-SVM model provides superior performance in handling linear inseparability compared to all other real soil layers. This demonstrates that the RBF-MSVM artificial intelligence algorithm can effectively classify and analyze electromagnetic wave signals in farmland soil.

Author Contributions: Conceptualization, Y.L. (Yuanhong Li) and Y.L. (Yangfan Luo); methodology, Y.L. (Yuanhong Li); software, Y.L. (Yangfan Luo); validation, C.W. (Congyue Wang); data curation, C.W. (Chaofeng Wang); writing—original draft preparation, Y.L. (Yuanhong Li); funding acquisition, Y.L. (Yuanhong Li); Supervision, Y.L. (Yubin Lan). All authors have read and agreed to the published version of the manuscript.

Funding: This work was financially supported by the Laboratory of Lingnan Modern Agriculture Project (Grant No. NT2021009); The Open Competition Program of the Top Ten Critical Priorities of Agricultural Science and Technology Innovation for the 14th Five-Year Plan of Guangdong Province (No. 2022SDZG03); Guangdong Basic and Applied Basic Research Foundation (Grant No. 2021A1515110554); China Postdoctoral Science Foundation (Grant No. 2022M721201); Guangdong

University Key Field (Artificial Intelligence) Special Project (No. 2019KZDZX1012) and the 111 Project (D18019); the National Natural Science Foundation of China (Grant No. 31901411).

Data Availability Statement: The data presented in this study are available on request from the corresponding author. The data are not publicly available due to privacy.

Acknowledgments: Much gratitude goes to Jieli Duan and Wenfeng Zhao for their contributions to this work.

Conflicts of Interest: The authors declare no conflict of interest.

References

1. Liu, X.; Dong, X.; Xue, Q.; Leskovar, D.I.; Jifon, J.; Butnor, J.R.; Marek, T. Ground penetrating radar (GPR) detects fine roots of agricultural crops in the field. *Plant Soil* **2018**, *423*, 517–531. [CrossRef]
2. Baili, J.; Lahouar, S.; Hergli, M.; Al-Qadi, I.L.; Besbes, K. GPR signal de-noising by discrete wavelet transform. *NDT E Int.* **2009**, *42*, 696–703. [CrossRef]
3. Bhuiyan, A.; Nath, B. Anti-personnel Mine Detection and Classification Using GPR Image. In Proceedings of the 18th International Conference on Pattern Recognition (ICPR'06), Hong Kong, China, 20–24 August 2006; IEEE: Piscataway, NJ, USA, 2006; Volume 2, pp. 1082–1085. [CrossRef]
4. Cui, Y.; Wang, L.; Xiao, J. Automatic Feature Recognition for GPR Image Processing. *Int. J. Comput. Inf. Eng.* **2010**, *61*, 176–179.
5. Ali, H.; Zaidi, A.F.A.; Meng, C.E.; Ahmad, M.R.; Amran, T.S.T.; Kanafiah, S.N.A.M.; Fook, C.Y.; Shukor, S.A.A.; Elshaikh, M. Shape classification of ground penetrating radar using discrete wavelet transform and principle component analysis. *IOP Conf. Ser. Mater. Sci. Eng.* **2019**, *705*, 012046. [CrossRef]
6. Taylor, C.D.; Castillo, J.P. On the Response of a Terminated Twisted-Wire Cable Excited by a Plane-Wave Electromagnetic Field. *IEEE Trans. Electromagn. Compat.* **1980**, *EMC-22*, 16–19. [CrossRef]
7. De-Shan, F.; Qian-Wei, D. GPR numerical simulation of full wave field based on UPML boundary condition of ADI-FDTD. *NDT E Int.* **2011**, *44*, 495–504. [CrossRef]
8. Teixeira, F.L.; Chew, W.C. Systematic derivation of anisotropic PML absorbing media in cylindrical and spherical coordinates. *IEEE Microw. Guid. Wave Lett.* **1997**, *7*, 371–373. [CrossRef]
9. Kilic, G.; Unluturk, M.S. Performance evaluation of the neural networks for moisture detection using GPR. *Nondestruct. Test. Eval.* **2014**, *29*, 283–296. [CrossRef]
10. Kilic, G.; Eren, L. Neural network based inspection of voids and karst conduits in hydro–electric power station tunnels using GPR. *J. Appl. Geophys.* **2018**, *151*, 194–204. [CrossRef]
11. Kobashigawa, J.S.; Youn, H.-S.; Iskander, M.F.; Yun, Z. Classification of Buried Targets Using Ground Penetrating Radar: Comparison Between Genetic Programming and Neural Networks. *IEEE Antennas Wirel. Propag. Lett.* **2011**, *10*, 971–974. [CrossRef]
12. Li, Y.; Zhao, Z.; Xu, W.; Liu, Z.; Wang, X. An effective FDTD model for GPR to detect the material of hard objects buried in tillage soil layer. *Soil Tillage Res.* **2019**, *195*, 104353. [CrossRef]
13. Núñez-Nieto, X.; Solla, M.; Gómez-Pérez, P.; Lorenzo, H. GPR Signal Characterization for Automated Landmine and UXO Detection Based on Machine Learning Techniques. *Remote Sens.* **2014**, *6*, 9729–9748. [CrossRef]
14. Rasol, M.; Pais, J.C.; Pérez-Gracia, V.; Solla, M.; Fernandes, F.M.; Fontul, S.; Ayala-Cabrera, D.; Schmidt, F.; Assadollahi, H. GPR monitoring for road transport infrastructure: A systematic review and machine learning insights. *Constr. Build. Mater.* **2022**, *324*, 126686. [CrossRef]
15. Ristić, A.; Bugarinović, Ž.; Vrtunski, M.; Govedarica, M. Point coordinates extraction from localized hyperbolic reflections in GPR data. *J. Appl. Geophys.* **2017**, *144*, 1–17. [CrossRef]
16. Frigui, H.; Gader, P. Detection and discrimination of landmines in ground-penetrating radar based on edge histogram de-scriptors. In *Detection and Remediation Technologies for Mines and Minelike Targets XI*; SPIE: Bellingham, WA, USA, 2006; Volume 6217, pp. 957–966.
17. Tantum, S.L.; Scott, W.R.; Morton, K.D.; Collins, L.M.; Torrione, P.A. Target Classification and Identification Using Sparse Model Representations of Frequency-Domain Electromagnetic Induction Sensor Data. *IEEE Trans. Geosci. Remote Sens.* **2012**, *51*, 2689–2706. [CrossRef]
18. Khalifa, A.B.; Frigui, H. A Multiple Instance Neuro-Fuzzy Inference System for Fusion of Multiple Landmine Detection Algorithms. In Proceedings of the 2015 IEEE International Geoscience and Remote Sensing Symposium (IGARSS), Milan, Italy, 26–31 July 2015; IEEE: Piscataway, NJ, USA, 2015; pp. 4312–4315. [CrossRef]
19. Bonomo, N.; De la Vega, M.; Martinelli, P.; Osella, A. Pipe-flange detection with GPR. *J. Geophys. Eng.* **2011**, *8*, 35–45. [CrossRef]
20. Lohlein, O.; Fritzsche, M. Classification of GPR data for mine detection based on hidden Markov models. In Proceedings of the Second International Conference on Detection of Abandoned Land Mines, Edinburgh, UK, 12–14 October 1998.
21. Manandhar, A.; Torrione, P.A.; Collins, L.M.; Morton, K.D. Multiple-Instance Hidden Markov Model for GPR-Based Landmine Detection. *IEEE Trans. Geosci. Remote Sens.* **2014**, *53*, 1737–1745. [CrossRef]

22. Yuksel, S.E.; Gader, P.D. Mixture of hmm experts with applications to landmine detection. In Proceedings of the 2012 IEEE International Geoscience and Remote Sensing Symposium, Munich, Germany, 22–27 July 2012; IEEE: Piscataway, NJ, USA, 2012; pp. 6852–6855.
23. Torrione, P.A.; Morton, K.D.; Sakaguchi, R.; Collins, L.M. Histograms of Oriented Gradients for Landmine Detection in Ground-Penetrating Radar Data. *IEEE Trans. Geosci. Remote Sens.* **2013**, *52*, 1539–1550. [CrossRef]
24. Bishop, C.M.; Nasrabadi, N.M. *Pattern Recognition and Machine Learning*; Springer: New York, NY, USA, 2006.
25. Karem, A.; Fadeev, A.; Frigui, H.; Gader, P. Comparison of different classification algorithms for landmine detection using GPR. In *Detection and Sensing of Mines, Explosive Objects, and Obscured Targets XV*; SPIE: Bellingham, WA, USA, 2010; Volume 7664, p. 76642. [CrossRef]
26. Cortes, C.; Vapnik, V. Support-vector networks. *Mach. Learn.* **1995**, *20*, 273–297. [CrossRef]
27. Pasolli, E.; Melgani, F.; Donelli, M. Automatic Analysis of GPR Images: A Pattern-Recognition Approach. *IEEE Trans. Geosci. Remote Sens.* **2009**, *47*, 2206–2217. [CrossRef]
28. Keskes, H.; Braham, A. Recursive Undecimated Wavelet Packet Transform and DAG SVM for Induction Motor Diagnosis. *IEEE Trans. Ind. Inform.* **2015**, *11*, 1059–1066. [CrossRef]
29. Dinh, K.; Zayed, T.; Moufti, S.; Shami, A.; Jabri, A.; Abouhamad, M.; Dawood, T.; Information, R. Clustering-Based Threshold Model for Condition Assessment of Concrete Bridge Decks with Ground-Penetrating Radar. *Transp. Res. Rec. J. Transp. Res. Board* **2015**, *2522*, 81–89. [CrossRef]
30. Xie, X.; Qin, H.; Yu, C.; Liu, L. An automatic recognition algorithm for GPR images of RC structure voids. *J. Appl. Geophys.* **2013**, *99*, 125–134. [CrossRef]
31. Dinh, K.; Gucunski, N.; Duong, T.H. An algorithm for automatic localization and detection of rebars from GPR data of concrete bridge decks. *Autom. Constr.* **2018**, *89*, 292–298. [CrossRef]
32. Karem, A.; Frigui, H. A comparative analysis of the SVM and K-NN to detect buried explosive objects using edge histogram features from GPR data. In *Detection and Sensing of Mines, Explosive Objects, and Obscured Targets XXIV*; SPIE: Bellingham, WA, USA, 2019; Volume 11012, pp. 95–108. [CrossRef]
33. Warren, C.; Giannopoulos, A.; Giannakis, I. gprMax: Open source software to simulate electromagnetic wave propagation for Ground Penetrating Radar. *Comput. Phys. Commun.* **2016**, *209*, 163–170. [CrossRef]
34. Li, Y.; Wang, X.; Zhao, Z.; Han, S.; Liu, Z. Lagoon water quality monitoring based on digital image analysis and machine learning esti-mators. *Water Res.* **2020**, *172*, 115471. [CrossRef] [PubMed]
35. Peplinski, N.R.; Ulaby, F.T.; Dobson, M.C. Dielectric properties of soils in the 0.3–1.3-GHz range. *IEEE Trans. Geosci. Remote Sens.* **1995**, *33*, 803–807. [CrossRef]
36. Khan, U.S.; Al-Nuaimy, W. Background removal from GPR data using eigenvalues. In Proceedings of the XIII Internarional Conference on Ground Penetrating Radar, Lecce, Italy, 21–25 June 2010; IEEE: Piscataway, NJ, USA, 2010; pp. 1–5.
37. Robinson, D.; Gardner, C.; Cooper, J. Measurement of relative permittivity in sandy soils using TDR, capacitance and theta probes: Comparison, including the effects of bulk soil electrical conductivity. *J. Hydrol.* **1999**, *223*, 198–211. [CrossRef]
38. Mapoka, K.O.M.; Birrell, S.J.; Tekeste, M.Z.; Steward, B.; Eisenmann, D. Using gprMax to Model Ground-Penetrating Radar (GPR) to Locate Corn Seed as an Attempt to Measure Planting Depth. *Trans. ASABE* **2019**, *62*, 673–686. [CrossRef]
39. Piltyay, S.; Bulashenko, A.; Herhil, Y.; Bulashenko, O. FDTD and FEM simulation of microwave waveguide polarizers. In Proceedings of the 2020 IEEE 2nd International Conference on Advanced Trends in Information Theory (ATIT), Kyiv, Ukraine, 25–27 November 2020; pp. 357–363.
40. Pedregosa, F.; Varoquaux, G.; Gramfort, A.; Michel, V.; Thirion, B.; Grisel, O.; Duchesnay, E. Scikit-learn: Machine learning in Python. *J. Mach. Learn. Res.* **2011**, *12*, 2825–2830.
41. Cole, J. High-accuracy Yee algorithm based on nonstandard finite differences: New developments and verifications. *IEEE Trans. Antennas Propag.* **2002**, *50*, 1185–1191. [CrossRef]
42. Dou, Q.; Wei, L.; Magee, D.R.; Cohn, A.G. Real-Time Hyperbola Recognition and Fitting in GPR Data. *IEEE Trans. Geosci. Remote Sens.* **2016**, *55*, 51–62. [CrossRef]
43. Pasolli, E.; Melgani, F.; Donelli, M.; Attoui, R.; de Vos, M. Automatic Detection and Classification of Buried Objects in GPR Images Using Genetic Algorithms and Support Vector Machines. In Proceedings of the IGARSS 2008–2008 IEEE International Geoscience and Remote Sensing Symposium, Boston, MA, USA, 7–11 July 2008; IEEE: Piscataway, NJ, USA, 2008; Volume 2, pp. II–525–II–528. [CrossRef]
44. Terrasse, G.; Nicolas, J.M.; Trouvé, E.; Drouet, É. Application of the curvelet transform for pipe detection in GPR images. In Proceedings of the 2015 IEEE International Geoscience and Remote Sensing Symposium (IGARSS), Milan, Italy, 26–31 July 2015; IEEE: Piscataway, NJ, USA, 2015; pp. 4308–4311.
45. Lian, F.Y.; Qing, L.I. Recognition method based on SVM for underground pipe diameter size in GPR map. *Inf. Electron. Eng.* **2011**, *9*, 403–408.
46. Rhoades, J.D.; Corwin, D.L. Determining Soil Electrical Conductivity-Depth Relations Using an Inductive Electromagnetic Soil Conductivity Meter. *Soil Sci. Soc. Am. J.* **1981**, *45*, 255–260. [CrossRef]
47. Porretta, R.; Bianchi, F. Profiles of relative permittivity and electrical conductivity from unsaturated soil water content models. *Ann. Geophys.* **2016**, *59*, G0320. [CrossRef]

48. Hui-Lin, Z.; Mao, T.; Xiao-Li, C. Feature extraction and classification of echo signal of ground penetrating radar. *Wuhan Univ. J. Nat. Sci.* **2005**, *10*, 1009–1012. [CrossRef]
49. Platt, J. Probabilistic outputs for support vector machines and comparisons to regularized likelihood methods. *Adv. Large Margin Classif.* **1999**, *10*, 61–74.
50. Ge, C.; Kasabov, N.; Liu, Z.; Yang, J. A spiking neural network model for obstacle avoidance in simulated prosthetic vision. *Inf. Sci.* **2017**, *399*, 30–42. [CrossRef]
51. Li, J.; Teng, Z.; Tang, Q.; Song, J. Detection and Classification of Power Quality Disturbances Using Double Resolution S-Transform and DAG-SVMs. *IEEE Trans. Instrum. Meas.* **2016**, *65*, 2302–2312. [CrossRef]
52. Zhou, W.; Wang, G.; Chen, X.; Chen, M.; Tian, M. Classification of Ground Penetrating Radar Echo Signals using Wavelet Packet and RBF. In Proceedings of the 2006 IEEE Conference on Radar, Verona, NY, USA, 24–27 April 2006. [CrossRef]
53. Lin, H.T.; Lin, C.J. A study on sigmoid kernels for SVM and the training of non-PSD kernels by SMO-type methods. *Neural Comput.* **2003**, *3*, 16.
54. Wu, T.F.; Lin, C.J.; Weng, R. Probability estimates for multi-class classification by pairwise coupling. *Adv. Neural Inf. Process. Syst.* **2003**, *16*, 20–25.
55. Faize, A.; Lahalal, F.; Atounti, M. Study and simulation of soil salinity evolution by Reflexw and GprMax. *Ann. Univ. Craiova-Math. Comput. Sci. Ser.* **2019**, *46*, 426–432.
56. El-Mahallawy, M.S.; Hashim, M. Material classification of underground utilities from GPR images using DCT-based SVM ap-proach. *IEEE Geosci. Remote Sens. Lett.* **2013**, *10*, 1542–1546. [CrossRef]
57. Guyon, I.; Boser, B.E.; Vapnik, V. Automatic capacity tuning of very large VC-dimension classifiers. In *Advances in Neural Infor-Mation Processing Systems*; MIT Press: Cambridge, MA, USA, 1993.